



Metallic Conduction and Ferromagnetism in $\text{MAI}_2\text{O}_4/\text{SrTiO}_3$ Spinel/Perovskite Heterostructures (M=Fe, Co, Ni)

Zhang, Yu ; Gan, Yulin; Zhang, Hongrui ; Zhang, Hui ; Norby, Poul; Shen, Baogen; Sun, Jirong; Chen, Yunzhong

Published in:
Applied Physics Letters

Link to article, DOI:
[10.1063/1.5063540](https://doi.org/10.1063/1.5063540)

Publication date:
2018

Document Version
Peer reviewed version

[Link back to DTU Orbit](#)

Citation (APA):

Zhang, Y., Gan, Y., Zhang, H., Zhang, H., Norby, P., Shen, B., Sun, J., & Chen, Y. (2018). Metallic Conduction and Ferromagnetism in $\text{MAI}_2\text{O}_4/\text{SrTiO}_3$ Spinel/Perovskite Heterostructures (M=Fe, Co, Ni). *Applied Physics Letters*, 113(26), [261603]. <https://doi.org/10.1063/1.5063540>

General rights

Copyright and moral rights for the publications made accessible in the public portal are retained by the authors and/or other copyright owners and it is a condition of accessing publications that users recognise and abide by the legal requirements associated with these rights.

- Users may download and print one copy of any publication from the public portal for the purpose of private study or research.
- You may not further distribute the material or use it for any profit-making activity or commercial gain
- You may freely distribute the URL identifying the publication in the public portal

If you believe that this document breaches copyright please contact us providing details, and we will remove access to the work immediately and investigate your claim.

Metallic Conduction and Ferromagnetism in $M\text{Al}_2\text{O}_4/\text{SrTiO}_3$ Spinel/Perovskite Heterostructures ($M = \text{Fe}, \text{Co}, \text{Ni}$)

Yu Zhang,^{1,3} Yulin Gan,² Hongrui Zhang,^{1,3} Hui Zhang,^{1,3} Poul Norby,² Baogen Shen,^{1,3} Jirong Sun,^{1,3, a)} and Yunzhong Chen^{2, a)}

¹Beijing National Laboratory for Condensed Matter Physics and Institute of Physics, Chinese Academy of Sciences, Beijing 100190, Peoples' Republic of China

²Department of Energy Conversion and Storage, Technical University of Denmark, Risø Campus, 4000 Roskilde, Denmark

³School of Physical Sciences, University of Chinese Academy of Sciences, Beijing 100049, Peoples' Republic of China

Electronic mail: jrsun@iphy.ac.cn; yunc@dtu.dk

Abstract:

Recently, a high mobility quasi-two-dimensional electron gas (q-2DEG) has been reported for the heterointerface between two insulating and nonmagnetic oxides of spinel γ -Al₂O₃ and perovskite SrTiO₃ (STO). Herein, we fabricated the epitaxial heterostructure with Al-based magnetic spinel oxide M Al₂O₄ ($M = \text{Fe, Co, Ni}$) on perovskite STO. Remarkably, all the M Al₂O₄ ($M = \text{Fe, Co, Ni}$) films exhibit ferromagnetic behavior up to room temperature. Although the FeAl₂O₄/STO is insulating, the NiAl₂O₄/STO and CoAl₂O₄/STO heterointerfaces are found to be highly metallic and exhibit anomalous Hall effect (AHE) at temperatures below 30 K. Their Hall mobility is as high as $3 \times 10^4 \text{ cm}^2\text{V}^{-1}\text{s}^{-1}$, comparable to that of γ -Al₂O₃/STO interface. There has been evidence of oxygen-vacancy-related magnetism in γ -Al₂O₃/STO at temperatures below 5 K, while the enhanced AHE in NiAl₂O₄/STO and CoAl₂O₄/STO likely comes from the magnetic proximity effect induced by the top ferromagnetic M Al₂O₄ spinel films.

The metallic interface between two insulating oxides, where a quasi-two-dimensional electron gas (q-2DEG) resides, provides a promising platform for the exploration of emergent phenomena.^{1,2} Its attractive physical properties, such as superconductivity,³ ferromagnetism,⁴ high electron mobility,⁵ strong gating field,^{6,7} quantum Hall effect,⁸ and photo excitation effect,^{9,10} have drawn extensive interest. So far, the isostructural perovskite-type interface, particularly LaAlO₃/SrTiO₃ (LAO/STO)¹ has been investigated intensively. However, the high mobility q-2DEG discovered at the non-isostructural interface between spinel γ -Al₂O₃ and perovskite STO remains underinvestigated.^{2,11–14} In addition to the remarkably high electron mobility ($1.4 \times 10^5 \text{ cm}^2 \text{ V}^{-1} \text{ s}^{-1}$ at 2 K), the spinel structure of γ -Al₂O₃ also provides the opportunity to introduce intrinsic ferromagnetism into the heterostructure, which remains unexplored.

Herein, we epitaxially grew three new heterostructures, consisting of $M\text{Al}_2\text{O}_4$ ($M = \text{Fe}, \text{Co}, \text{Ni}$) top films and (001)-oriented TiO₂-terminated STO substrates, and investigated their interfacial conduction and ferromagnetism. Remarkably, all the $M\text{Al}_2\text{O}_4$ ($M = \text{Fe}, \text{Co}, \text{Ni}$) films exhibit ferromagnetic behavior up to room temperature. We further found that the NiAl₂O₄/STO and CoAl₂O₄/STO interfaces are metallic and ferromagnetic at low temperatures, as indicated by the appearance of anomalous Hall effect (AHE). The AHE of the $M\text{Al}_2\text{O}_4$ /STO interfaces ($M = \text{Ni}, \text{Co}$) remains sizable up to 30 K, in contrast to γ -Al₂O₃/STO which shows AHE below 5 K. Moreover, the anomalous Hall resistance (R_{AHE}) undergoes a negative to positive sign change when the top film of the heterostructure changes from γ -Al₂O₃ to $M\text{Al}_2\text{O}_4$. We proposed that the AHE in γ -Al₂O₃/STO is due to the oxygen vacancies induced ferromagnetism in proximity to the STO surface, while the AHE in NiAl₂O₄/STO and CoAl₂O₄/STO probably comes from the magnetic proximity effect induced by the ferromagnetic $M\text{Al}_2\text{O}_4$ spinel films. Different from NiAl₂O₄/STO and CoAl₂O₄/STO interfaces, FeAl₂O₄/STO is insulating.

Films were grown on TiO₂-terminated STO single crystal substrates (5 mm × 5 mm × 0.5 mm in dimensions) by pulsed laser deposition using a KrF laser with a wavelength of 248 nm. During deposition, the substrate temperature was maintained at 650 °C and the oxygen pressure was kept at 1×10⁻⁵ mbar. The laser fluence was 2 Jcm⁻² and the repetition rate was 1 Hz. The target-substrate distance was fixed at 5 cm. After deposition, the samples were cooled to room temperature without changing oxygen pressure. For the γ -Al₂O₃ deposition, a commercial Al₂O₃ single crystal target was used. M Al₂O₄ (M = Fe, Co, Ni) ceramic targets were adopted for other films. These targets were prepared by sintering the mixture of appropriate amounts of Al₂O₃ with Fe₂O₃, Co₃O₄ and NiO powders first, at 1200 °C for 10 h and then, after pressing, at 1350 °C for 36 h. The film growth rate is approximate 0.08 Å/s. The epitaxial growth of the crystalline films was confirmed by both reflection high-energy electron diffraction (RHEED) and high-resolution X-ray diffraction (XRD) measurements. Heterostructures with 4 nm thickness top films are employed for transport and magnetic measurements. While, heterostructures with 40 nm top films are used for XRD measurements. Ultrasonic Al wire bonding was used to get electric connection, and the van der Pauw geometry was adopted.

Fig. 1(a) is a schematic illustration of the spinel/perovskite (M Al₂O₄/STO) oxide heterostructure. The epitaxial growth of spinel M Al₂O₄ (M = Fe, Co, Ni) films on perovskite STO substrate is due to their compatible oxygen sub-lattice, as the lattice parameter of M Al₂O₄ is about twice that of STO.² Although γ -Al₂O₃ and STO show a good lattice match (1%), NiAl₂O₄, CoAl₂O₄, and FeAl₂O₄ exhibit larger lattice mismatch with STO substrate (> 3%) as summarized in Table I. Consequently, the γ -Al₂O₃ film can be epitaxially grown on STO (001) substrate with a persistent layer-by-layer two-dimensional growth mode as confirmed by RHEED and high-resolution transmission electron microscopy,^{13,15} while the NiAl₂O₄, CoAl₂O₄, and FeAl₂O₄ films show 3D island growth mode. Despite of this, the epitaxial growth of NiAl₂O₄, CoAl₂O₄, and FeAl₂O₄ films

with the thickness of 40 nm on STO is confirmed by the XRD measurements. As shown in Figs. 1(b), for the $\theta - 2\theta$ scan in the region of $10^\circ - 80^\circ$, (004) spinel Bragg peaks is observed on the left side of the corresponding STO peaks of (002). The out-of-line lattice parameters of $\gamma\text{-Al}_2\text{O}_3$, NiAl_2O_4 , CoAl_2O_4 , and FeAl_2O_4 films determined by XRD are 8.02, 8.03, 8.08, and 8.16 Å, respectively. This indicates that all the $M\text{Al}_2\text{O}_4$ films are well strain-relaxed. In addition, for the films of NiAl_2O_4 and FeAl_2O_4 , impurity phase of $M\text{AlO}_2$ ($M = \text{Ni, Fe}$) at 16.6° is detected. For NiAl_2O_4 film, an extra impurity phase of Ni (200) crystal phase at 51.7° is also observed. These impurity phases could stem from the reduction environment of low oxygen pressure (1×10^{-5} mbar) and high temperature (650°C) adopted during the film deposition.¹⁶ However, the low diffraction intensity indicates that the amount of these impurities is rather low. Notably, these impurity phases survive after the post annealing at 300°C in 1 bar oxygen for 3 hours, meanwhile, the interface becomes insulating. Therefore, such impurity phases contribute negligibly to the interface conduction as discussed later. This is also consistent with the fact that $M\text{Al}_2\text{O}_4$ ($M = \text{Fe, Co, Ni}$) films grown on $(\text{LaAlO}_3)_{0.3}(\text{Sr}_2\text{TaAlO}_6)_{0.7}$ (LSAT) substrates are insulating in nature (see in Supplemental Material S1). Fig. 1(c) shows the Rocking curves of the (004) spinel films grown on STO substrates. The full widths at half maximum (FWHM) of the curves determined by Gaussian fitting are shown in Table I. All $M\text{Al}_2\text{O}_4$ ($M = \text{Fe, Co, Ni}$) films display good crystallinity. In addition, comparing to $M\text{Al}_2\text{O}_4$ spinel films, the relatively larger FWHM (0.21°) of $\gamma\text{-Al}_2\text{O}_3$ film might be due to its less ordered crystallographic structure which contains cation vacancies.¹⁷

Transport measurements show that $\text{FeAl}_2\text{O}_4/\text{STO}$ is highly insulating. However, the metallic conduction is obtained in $\gamma\text{-Al}_2\text{O}_3/\text{STO}$, $M\text{Al}_2\text{O}_4/\text{STO}$ ($M = \text{Ni, Co}$) heterostructures, as shown in Fig. 2(a). Comparing to $\gamma\text{-Al}_2\text{O}_3/\text{STO}$ whose sheet resistance (R_s) is $278 \Omega/\square$ at room temperature, the $\text{NiAl}_2\text{O}_4/\text{STO}$ and $\text{CoAl}_2\text{O}_4/\text{STO}$ have smaller R_s which are $57.8 \Omega/\square$ and $138 \Omega/\square$, respectively. Figs. 2(b)-(d) display the Hall resistance (R_{xy}) of $\gamma\text{-Al}_2\text{O}_3/\text{STO}$, $\text{NiAl}_2\text{O}_4/\text{STO}$ and $\text{CoAl}_2\text{O}_4/\text{STO}$ as

a function of magnetic field (B) in the temperature range from 295 to 2 K. When temperature is high ($T > 100$ K), R_{xy} varies linearly with applied field for all samples. This is the typical behavior of the normal Hall effect (NHE). Cooling the samples to 100 K, R_{xy} shows nonlinear dependence on magnetic field. In the meanwhile, the magnetic field-dependent magnetoresistance ($MR = (R_{xx}(B)/R_{xx}(B=0)) - 1$) traces follow a bell-like shape, where MR - B displays a U-shape at low field, and shift to a bell-shape at high field. These features suggest that the conductivity comes from two or more carriers as previously reported by Joshua *et al.*¹⁸ and Kim *et al.*¹⁹, and can be fitted by a two-band model (see Supplemental Material S2). However, the R_{xy} exhibits a stronger curvature in the low-field range when further cooled below a critical temperature of approximately 30 K, which is beyond the capture of the two-band model. To describe the R_{xy} - B relation at $T < 30$ K, we adopted an extended two-band model that combines the two-band conduction-dominated NHE with an AHE as reported before^{20,21} (see Supplemental Material S2):

$$R_{xy} = R_{NHE} + R_{AHE} = R_{NHE} + \alpha L\left(\frac{mB}{k_B T}\right) \quad (1)$$

where R_{NHE} and R_{AHE} represent the Hall resistance from two-band conduction and AHE, respectively. The Langevin function L is introduced to simulate the step-shaped AHE curve in form, α is a scale factor, and m is magnetic moment.

Fig. 2(e) displays the determination of the anomalous Hall resistance, R_{AHE} , from R_{xy} . The results of *eq. 1* (thin black line) well reproduce the measured R_{xy} (thick green line). Basically, the normal Hall resistance (R_{NHE}) varies smoothly with B in the whole field range, with slightly but identifiable curve bending. In contrast, R_{AHE} is constant in high-field range and undergoes a drastic change as B sweeps through zero field. It also becomes clear that AHE appears below 5 K for γ - $\text{Al}_2\text{O}_3/\text{STO}$, and 30 K for both $\text{NiAl}_2\text{O}_4/\text{STO}$ and $\text{CoAl}_2\text{O}_4/\text{STO}$. Based on the R_{NHE} in *eq. 1*, the temperature-dependent density (n_s) and Hall mobility (μ) of the carriers confined in heterostructures

can be deduced (Figs. 2(f)-(g)). The n_s of q-2DEGs is nearly constant from 295 K to 2 K. At 2 K, the γ -Al₂O₃/STO possesses the lowest n_s with a value of $3 \times 10^{15} \text{ cm}^{-2}$. The NiAl₂O₄/STO heterointerface has the highest n_s ($2.2 \times 10^{16} \text{ cm}^{-2}$) which is higher than γ -Al₂O₃/STO by a factor of 7. The n_s of CoAl₂O₄/STO is $9.8 \times 10^{15} \text{ cm}^{-2}$. These extremely high carrier densities indicate that 3D STO bulk conduction contributes to the measured conductivity. With regards to the μ , these three heterostructures have comparable values in the range of $2.7 - 3.4 \times 10^4 \text{ cm}^2\text{V}^{-1}\text{s}^{-1}$ at 2 K, also consistent with the mobility for bulk STO.^{1,13} It is noteworthy that the FeAl₂O₄/STO grown under the same condition with NiAl₂O₄/STO and CoAl₂O₄/STO is highly insulating. This means that the Al-based spinel/perovskite interface is extremely sensitive to the introduction of the magnetic ions.

The metallic conduction in STO-based heterostructures comes from electrons located on the STO side. The high n_s in γ -Al₂O₃/STO and $M\text{Al}_2\text{O}_4/\text{STO}$ ($M = \text{Ni, Co}$) could result from the formation of oxygen vacancies in STO due to interfacial redox reactions.^{2,13,15,22} However, the insulating FeAl₂O₄/STO heterointerface might stem from two reasons. On the one hand, the Fe-based oxide has poor ability to reduce STO substrate during the film deposition.²³ On the other hand, the band gap of FeAl₂O₄ (1.78 eV²⁴) is much lower than that of STO (3.2 eV), any reconstructed electrons tend to accumulate in the spinel films rather than transferring to the heterointerface.²⁵

Figs. 3(a)-(c) show the R_{AHE} variation with respect to B at different temperatures for γ -Al₂O₃/STO, $M\text{Al}_2\text{O}_4/\text{STO}$ ($M = \text{Ni, Co}$). The R_{AHE} of γ -Al₂O₃/STO has the same sign to B , while that of $M\text{Al}_2\text{O}_4/\text{STO}$ ($M = \text{Ni, Co}$) are opposite to B . Similar crossover in the sign of R_{AHE} has also been observed between SrRuO₃ and La_{1-x}Sr_xCoO₃ ($x=0.17$) crystals.²⁶ But the explanation for such phenomenon remains open, which could result from the intrinsic different origins of the magnetism. Moreover, in the magnetic saturation state, such as under $B = -10 \text{ T}$ at 2 K, R_{AHE} is as large as $0.013 \text{ } \Omega$ for γ -Al₂O₃/STO, while it is $0.008 \text{ } \Omega$ for NiAl₂O₄/STO and $0.012 \text{ } \Omega$ for CoAl₂O₄/STO. Fig. 3(d)

summarizes the R_{AHE} for these three heterointerfaces as a function of temperature. Clearly, the AHE appears at $T \leq 30$ K for $M\text{Al}_2\text{O}_4/\text{STO}$ ($M = \text{Ni}, \text{Co}$), whereas, only below 5 K for $\gamma\text{-Al}_2\text{O}_3/\text{STO}$ as discussed before. Shortly, the AHE of the $M\text{Al}_2\text{O}_4/\text{STO}$ ($M = \text{Ni}, \text{Co}$) is dramatically different from that of $\gamma\text{-Al}_2\text{O}_3/\text{STO}$.

In order to uncover the origin of AHE in $\gamma\text{-Al}_2\text{O}_3/\text{STO}$ and $M\text{Al}_2\text{O}_4/\text{STO}$ ($M = \text{Ni}, \text{Co}$) heterointerfaces, magnetic measurements were performed by superconducting quantum interference device (SQUID) magnetometer (as shown in Fig. 3(e)). Remarkably, these three $M\text{Al}_2\text{O}_4/\text{STO}$ ($M = \text{Fe}, \text{Co}, \text{Ni}$) heterostructures exhibit unexpected ferromagnetic properties up to room temperature. Notably, the CoAl_2O_4 and FeAl_2O_4 show spin-glass-like ground states in bulk below the Curie-Weiss temperatures (5 K for CoAl_2O_4 and 12 K for FeAl_2O_4),^{27,28} and the NiAl_2O_4 is paramagnetic.²⁹ In the meantime, the ferromagnetism of $\gamma\text{-Al}_2\text{O}_3/\text{STO}$ is very weak (see Supplementary Material S3). At room temperature (inset of Fig. 3(e)), the magnetizations of FeAl_2O_4 , CoAl_2O_4 and NiAl_2O_4 are 135.3, 76.4 and 69.4 emu/cm³ when $B = 6$ T, respectively, which are much lower than the magnetization of Fe_3O_4 (about 480 emu/cm³ at room temperature).³⁰ When the temperature is 10 K, FeAl_2O_4 has the strongest magnetization, which is as large as 291.3 emu/cm³ at $B = 6$ T, while CoAl_2O_4 and NiAl_2O_4 have comparable magnetization, which are 196.2 and 177.9 emu/cm³, respectively. As for the interface between $\gamma\text{-Al}_2\text{O}_3$ and STO, the conduction comes from the oxygen vacancies, which could result in ferromagnetism, thus, the AHE as the origin of the ferromagnetism in LAO/STO.^{31–33} These oxygen vacancies not only induce a complex multi-orbital reconstruction thus the mobile q-2DEG, but also result the spin splitting of the electronic states, giving rise to localized Ti 3d electrons thus magnetism. Salluzzo *et al.*³³ experimentally proved that the oxygen vacancies play a decisive role in the interfacial magnetism in LAO/STO. Whereas, the much higher upper limit temperature (30 K) of AHE observed in our

$M\text{Al}_2\text{O}_4/\text{STO}$ ($M = \text{Ni}, \text{Co}$) heterostructures than that of $\gamma\text{-Al}_2\text{O}_3/\text{STO}$ (5 K) indicates that the oxygen-vacancy-related AHE in $M\text{Al}_2\text{O}_4/\text{STO}$ is relatively weak.

It has also been suggested that interdiffusion of magnetic cations into STO could result in a similar transport behavior in manganite-buffered LAO/STO heterostructure.²⁰ Since the interdiffusion of cations is also a common phenomenon in the spinel/perovskite heterostructure, such as $\gamma\text{-Al}_2\text{O}_3/\text{STO}$.² Therefore, we cannot rule out the possibility of the interdiffusion of magnetic ions into STO as a possible origin of AHE at $M\text{Al}_2\text{O}_4/\text{STO}$ heterointerfaces. However, such interdiffusion of magnetic ions into STO could result in Kondo effect, which is absent here. Finally, since the top films are found to be ferromagnetic, we therefore assume that the AHE in $M\text{Al}_2\text{O}_4/\text{STO}$ ($M = \text{Ni}, \text{Co}$) comes from the magnetism induced by a magnetic proximity effect as reported for the EuTiO_3 -buffered LAO/STO heterostructure.³⁴

In summary, we epitaxially grown $M\text{Al}_2\text{O}_4/\text{STO}$ ($M = \text{Fe}, \text{Co}, \text{Ni}$) heterostructures in comparison to the $\gamma\text{-Al}_2\text{O}_3/\text{STO}$ heterostructure. Remarkably, all the $M\text{Al}_2\text{O}_4$ ($M = \text{Fe}, \text{Co}, \text{Ni}$) films exhibit ferromagnetic behavior up to room temperature. The heterointerface of $\text{FeAl}_2\text{O}_4/\text{STO}$ is highly insulating. In contrast, the $\text{NiAl}_2\text{O}_4/\text{STO}$ and $\text{CoAl}_2\text{O}_4/\text{STO}$ are metallic conducting. AHE is observed in most of the metallic interfaces of $\gamma\text{-Al}_2\text{O}_3/\text{STO}$, $\text{NiAl}_2\text{O}_4/\text{STO}$ and $\text{CoAl}_2\text{O}_4/\text{STO}$. While the AHE in $\gamma\text{-Al}_2\text{O}_3/\text{STO}$ is likely due to the magnetism induced by oxygen vacancies, the AHE in $\text{NiAl}_2\text{O}_4/\text{STO}$ and $\text{CoAl}_2\text{O}_4/\text{STO}$ most likely comes from the magnetic proximity effect induced by the top ferromagnetic spinel films.

Supplementary Material

See supplementary material for XRD data of NiAl_2O_4 films prepared under different oxygen pressures, on different substrates (STO, LSAT) and after the post oxygen annealing; Two-band model fitting of interface conduction; Magnetization of spinel/perovskite heterostructures.

Acknowledgements:

We acknowledge the support of the National Basic Research of China (No. 2016YFA0300701), the National Natural Science Foundation of China (Nos. 11520101002 and 51590880), and the Key Program of the Chinese Academy of Sciences.

References:

- ¹ A. Ohtomo and H.Y. Hwang, *Nature* **427**, 423 (2004).
- ² Y.Z. Chen, N. Bovet, F. Trier, D. V. Christensen, F.M. Qu, N.H. Andersen, T. Kasama, W. Zhang, R. Giraud, J. Dufouleur, T.S. Jespersen, J.R. Sun, A. Smith, J. Nygård, L. Lu, B. Büchner, B.G. Shen, S. Linderoth, and N. Pryds, *Nat. Commun.* **4**, 1371 (2013).
- ³ N. Reyren, S. Thiel, A.D. Caviglia, L. Fitting Kourkoutis, G. Hammerl, C. Richter, C.W. Schneider, T. Kopp, A.-S. Rüetschi, D. Jaccard, M. Gabay, D.A. Muller, J.-M. Triscone, and J. Mannhart, *Science* **317**, 1196 (2007).
- ⁴ A. Brinkman, M. Huijben, M. Van Zalk, J. Huijben, U. Zeitler, J.C. Maan, W.G. Van Der Wiel, G. Rijnders, D.H.A. Blank, and H. Hilgenkamp, *Nat. Mater.* **6**, 493 (2007).
- ⁵ Y.Z. Chen, F. Trier, T. Wijnands, R.J. Green, N. Gauquelin, R. Egoavil, D. V. Christensen, G. Koster, M. Huijben, N. Bovet, S. Macke, F. He, R. Sutarto, N.H. Andersen, J.A. Sulpizio, M. Honig, G.E.D.K. Prawiroatmodjo, T.S. Jespersen, S. Linderoth, S. Ilani, J. Verbeeck, G. Van Tendeloo, G. Rijnders, G.A. Sawatzky, and N. Pryds, *Nat. Mater.* **14**, 801 (2015).
- ⁶ W. Niu, Y. Zhang, Y. Gan, D. V. Christensen, M. V. Soosten, E.J. Garcia-Suarez, A. Riisager, X. Wang, Y. Xu, R. Zhang, N. Pryds, and Y. Chen, *Nano Lett.* **17**, 6878 (2017).

- ⁷ W.N. Lin, J.F. Ding, S.X. Wu, Y.F. Li, J. Lourembam, S. Shannigrahi, S.J. Wang, and T. Wu, *Adv. Mater. Interfaces* **1**, 1300001 (2014).
- ⁸ F. Trier, G.E.D.K. Prawiroatmodjo, Z. Zhong, D.V. Christensen, M. Von Soosten, A. Bhowmik, J.M.G. Lastra, Y. Chen, T.S. Jespersen, and N. Pryds, *Phys. Rev. Lett.* **117**, 096804 (2016).
- ⁹ Y. Lei, Y. Li, Y.Z. Chen, Y.W. Xie, Y.S. Chen, S.H. Wang, J. Wang, B.G. Shen, N. Pryds, H.Y. Hwang, and J.R. Sun, *Nat. Commun.* **5**, 5554 (2014).
- ¹⁰ H. Yan, Z. Zhang, S. Wang, H. Zhang, C. Chen, and K. Jin, *ACS Appl. Mater. Interfaces* **9**, 39011 (2017).
- ¹¹ D. V. Christensen, M. von Soosten, F. Trier, T.S. Jespersen, A. Smith, Y. Chen, and N. Pryds, *Adv. Electron. Mater.* **3**, 1700026 (2017).
- ¹² P. Schütz, F. Pfaff, P. Scheiderer, Y.Z. Chen, N. Pryds, M. Gorgoi, M. Sing, and R. Claessen, *Phys. Rev. B* **91**, 165118 (2015).
- ¹³ Y.Z. Chen, N. Bovet, T. Kasama, W.W. Gao, S. Yazdi, C. Ma, N. Pryds, and S. Linderoth, *Adv. Mater.* **26**, 1462 (2014).
- ¹⁴ S.W. Lee, Y. Liu, J. Heo, and R.G. Gordon, *Nano Lett.* **12**, 4775 (2012).
- ¹⁵ T.Q. Ngo, N.J. Goble, A. Posadas, K.J. Kormondy, S. Lu, M.D. McDaniel, J. Jordan-Sweet, D.J. Smith, X.P.A. Gao, A.A. Demkov, and J.G. Ekerdt, *J. Appl. Phys.* **118**, 115303 (2015).
- ¹⁶ Y.S. Jung, W.L. Yoon, Y.S. Seo, and Y.W. Rhee, *Catal. Commun.* **26**, 103 (2012).
- ¹⁷ B. Ealet, M.H. Elyakhloufi, E. Gillet, and M. Ricci, *Thin Solid Films* **250**, 92 (1994).
- ¹⁸ A. Joshua, S. Pecker, J. Ruhman, E. Altman, and S. Ilani, *Nat. Commun.* **3**, 1129 (2012).

- ¹⁹ J.S. Kim, S.S.A. Seo, M.F. Chisholm, R.K. Kremer, H.U. Habermeier, B. Keimer, and H.N. Lee, Phys. Rev. B **82**, 201407 (2010).
- ²⁰ H.R. Zhang, Y. Zhang, H. Zhang, J. Zhang, X. Shen, X.X. Guan, Y.Z. Chen, R.C. Yu, N. Pryds, Y.S. Chen, B.G. Shen, and J.R. Sun, Phys. Rev. B **96**, 195167 (2017).
- ²¹ F. Gunkel, C. Bell, H. Inoue, B. Kim, A.G. Swartz, T.A. Merz, Y. Hikita, S. Harashima, H.K. Sato, M. Minohara, S. Hoffmann-Eifert, R. Dittmann, and H.Y. Hwang, Phys. Rev. X **6**, 031035 (2016).
- ²² K.J. Kormondy, A.B. Posadas, T.Q. Ngo, S. Lu, N. Goble, J. Jordan-Sweet, X.P.A. Gao, D.J. Smith, M.R. McCartney, J.G. Ekerdt, and A.A. Demkov, J. Appl. Phys. **117**, 095303 (2015).
- ²³ A.B. Posadas, K.J. Kormondy, W. Guo, P. Ponath, J. Geler-Kremer, T. Hadamek, and A.A. Demkov, J. Appl. Phys. **121**, 105302 (2017).
- ²⁴ H.Y. Mu, F.T. Li, X.T. An, R.H. Liu, Y.L. Li, X. Qian, and Y.Q. Hu, Phys. Chem. Chem. Phys. **19**, 9392 (2017).
- ²⁵ W. Niu, W. Liu, M. Gu, Y. Chen, X. Zhang, M. Zhang, Y. Chen, J. Wang, J. Du, F. Song, X. Pan, N. Pryds, X. Wang, P. Wang, Y. Xu, Y. Chen, and R. Zhang, Adv. Electron. Mater. **4**, 1800055 (2018).
- ²⁶ T. Miyasato, N. Abe, T. Fujii, A. Asamitsu, S. Onoda, Y. Onose, N. Nagaosa, and Y. Tokura, Phys. Rev. Lett. **99**, 086602 (2007).
- ²⁷ G.M. Kalvius, A. Krimmel, O. Hartmann, F.J. Litterst, R. Wäppling, V. Tsurkan, and A. Loidl, Phys. B Condens. Matter **404**, 660 (2009).

- ²⁸ N. Tristan, J. Hemberger, A. Krimmel, H.A. Krug Von Nidda, V. Tsurkan, and A. Loidl, *Phys. Rev. B* **72**, 174404 (2005).
- ²⁹ S. Kamali, *J. Magn. Magn. Mater.* **433**, 155 (2017).
- ³⁰ Y.Z. Chen, J.R. Sun, Y.N. Han, X.Y. Xie, J. Shen, C.B. Rong, S.L. He, and B.G. Shen, *J. Appl. Phys.* **103**, 07D703 (2008).
- ³¹ N. Pavlenko, T. Kopp, E.Y. Tsymbal, G.A. Sawatzky, and J. Mannhart, *Phys. Rev. B* **85**, 020407 (2012).
- ³² N. Pavlenko, T. Kopp, E.Y. Tsymbal, J. Mannhart, and G.A. Sawatzky, *Phys. Rev. B* **86**, 064431 (2012).
- ³³ M. Salluzzo, S. Gariglio, D. Stornaiuolo, V. Sessi, S. Rusponi, C. Piamonteze, G.M. De Luca, M. Minola, D. Marré, A. Gadaleta, H. Brune, F. Nolting, N.B. Brookes, and G. Ghiringhelli, *Phys. Rev. Lett.* **111**, 087204 (2013).
- ³⁴ D. Stornaiuolo, C. Cantoni, G.M. De Luca, R. Di Capua, E. Di Gennaro, G. Ghiringhelli, B. Jouault, D. Marrè, D. Massarotti, F.M. Granozio, I. Pallecchi, C. Piamonteze, S. Rusponi, F. Tafuri, and M. Salluzzo, *Nat. Mater.* **15**, 278 (2016).
- ³⁵ R.S. Zhou and R.L. Snyder, *Acta Crystallogr. Sect. B* **47**, 617 (1991).
- ³⁶ Y.S. Han, J.B. Li, X.S. Ning, and B. Chi, *J. Am. Ceram. Soc.* **87**, 1347 (2004).
- ³⁷ M.G. Brik, A. Suchocki, and A. Kamińska, *Inorg. Chem.* **53**, 5088 (2014).
- ³⁸ A. Walsh, S.H. Wei, Y. Yan, M.M. Al-Jassim, J.A. Turner, M. Woodhouse, and B.A. Parkinson, *Phys. Rev. B* **76**, 165119 (2007).

³⁹ M. Yazdanmehr, S.J. Asadabadi, A. Nourmohammadi, M. Ghasemzadeh, and M. Rezvanian, *Nanoscale Res. Lett.* **7**, 448 (2012).

⁴⁰ M.E. Gouda and W.A.A. Bayoumy, *Int. J. Sci. Eng. Res.* **6**, 328 (2015).

Table I. Lattice parameters of γ -Al₂O₃, M Al₂O₄ (M = Fe, Co, Ni) in bulk from reports and in film shown in text deduced by XRD data, their mismatches with STO substrate, the full widths at half maximum (FWHM) of Rocking curves for the films, their band gaps, and conductivities of the STO-based heterointerfaces at room temperature:

	γ -Al ₂ O ₃	NiAl ₂ O ₄	CoAl ₂ O ₄	FeAl ₂ O ₄
Bulk Lattice Parameter	7.911 ³⁵	8.05 ^{36,37}	8.10 ^{28,38}	8.16 ^{28,38}
Mismatch with STO Substrate (%)	1.3	3.1	3.7	4.5
FWHM of Film (deg.)	0.214	0.089	0.086	0.087
Film Lattice Parameter	8.02	8.03	8.08	8.16
Band Gap (eV)	8.7 ^{17,39}	3.4 ⁴⁰	3.6 ⁴⁰	1.78 ²⁴
Room Temperature $R_s(\Omega/\square)$	278	57.8	138	$> 10^8$

Figure captions:

FIG. 1 (a) A schematic sketch of the spinel/perovskite ($M\text{Al}_2\text{O}_4/\text{STO}$) oxide heterostructure ($M = \text{Fe, Co, Ni}$). Lattice structures of the spinel and perovskite are shown below. The box represents one unit cell, the lattice parameter of $M\text{Al}_2\text{O}_4$ is about twice that of STO. (b) X-ray diffraction (XRD) $\theta - 2\theta$ scan of the $\gamma\text{-Al}_2\text{O}_3$, NiAl_2O_4 , CoAl_2O_4 , and FeAl_2O_4 films grown on TiO_2 -terminated STO substrates. The inset shows the XRD θ - 2θ scan around the STO (002) reflection. (c) Omega Rocking curves of the epitaxial films in spinel/perovskite heterostructures.

FIG. 2 (a) Temperature-dependent sheet resistances (R_s) of q-2DEGs in $\gamma\text{-Al}_2\text{O}_3/\text{STO}$, $\text{NiAl}_2\text{O}_4/\text{STO}$ and $\text{CoAl}_2\text{O}_4/\text{STO}$ heterostructures. (b) - (d) Magnetic dependence of Hall resistances (R_{xy}) in the three heterostructures at different temperatures, respectively. (e) Example for the determination of normal Hall effect (NHE) and anomalous Hall effect (AHE) from the total Hall effect for $\text{NiAl}_2\text{O}_4/\text{STO}$ at 2K. Measured and calculated results are presented as thick green and thin black lines, respectively. Temperature dependence of (f) sheet carrier densities, n_s , and (g) Hall mobilities, μ , in these heterostructures.

FIG. 3 (a)-(c) Anomalous Hall resistances, R_{AHE} , in $\gamma\text{-Al}_2\text{O}_3/\text{STO}$, $\text{NiAl}_2\text{O}_4/\text{STO}$ and $\text{CoAl}_2\text{O}_4/\text{STO}$ heterostructures as a function of magnetic field at different temperatures. (d) Anomalous Hall resistances (at $B = -10$ T) as a function of temperatures for these three samples. (e) Magnetization curves as a function of magnetic field (M-H) for $\gamma\text{-Al}_2\text{O}_3$ and $M\text{Al}_2\text{O}_4$ ($M = \text{Fe, Co, Ni}$) films with a thickness of 4 nm measured at 10 K. The inset is the M-H measured at 300 K.

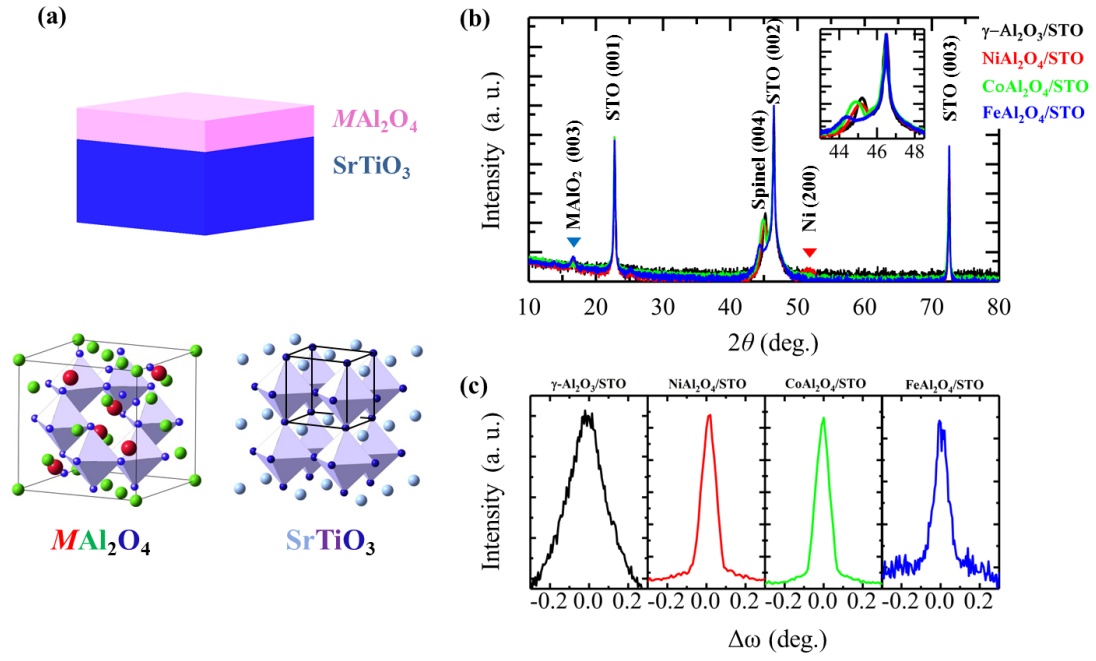


FIG. 1

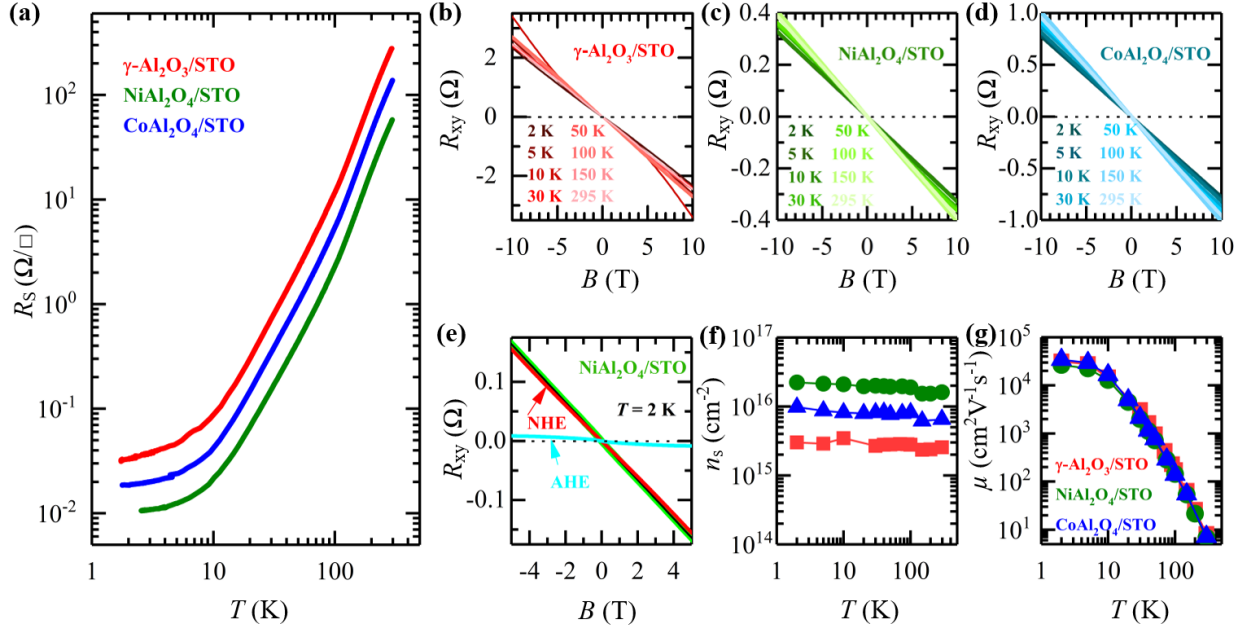


FIG.2

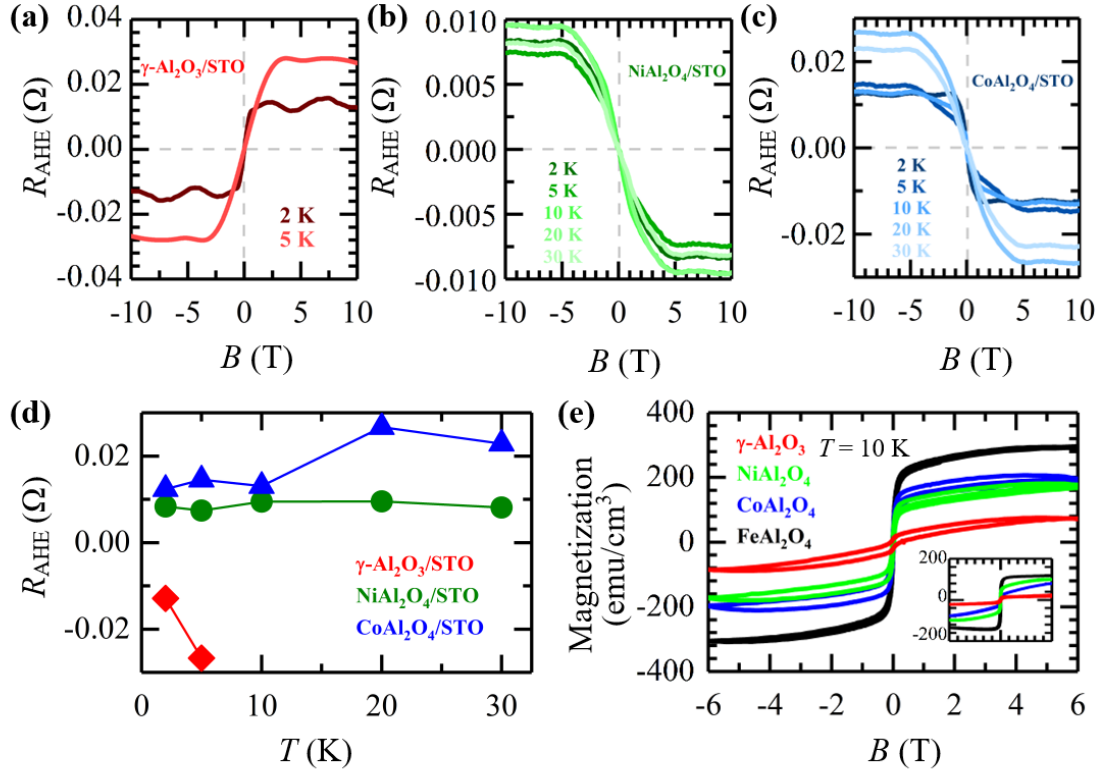


FIG.3